Unraveling the Multiple Effects Originating the Increased Oxidative Photoactivity of {001}-Facet Enriched Anatase TiO_2

Michela Maisano,[†] Maria Vittoria Dozzi,[†] Mauro Coduri,[‡] Luca Artiglia,[§] Gaetano Granozzi,[§] and Elena Selli*[†]*

[†] Dipartimento di Chimica, Università degli Studi di Milano, via Golgi 19, I-20133 Milano, Italy

[‡] CNR-IENI Institute for Energetics and Interphases, Corso Promessi Sposi 29, I-23900 Lecco, Italy

[§] Dipartimento di Scienze Chimiche, Università degli Studi di Padova, via Marzolo 1, I-35131 Padova, Italy

ABSTRACT: Crystal shape control on a series of anatase photocatalysts was achieved by varying the amount of HF employed as a capping agent in their hydrothermal synthesis. A systematic comparison between their physico-chemical properties, determined by several complementary surface and bulk techniques, before and after thermal treatment at 500 °C, allowed one to discern the influence of the relative amount of exposed {001} crystal facets among a series of effects simultaneously affecting their oxidative photocatalytic activity. The results of both formic acid and terephthalic acid photooxidation test reactions point to the primary role played by calcination in making {001} facets effectively photoactive. Annealing not only removes most of the residual fluorine capping agent from the photocatalyst surface, thus favoring substrate adsorption, but also produces morphological modifications to a crystal packing which makes accessible a larger portion of surface {001} facets, due to unpiling of plate-like crystals. The photocatalyst bearing the highest amount of exposed {001} facets (60%) shows the highest photoactivity in both the direct and the $^{\bullet}$OH radical mediated photocatalytic test reaction.

KEYWORDS: *photocatalysis, anatase {001} facets; surface fluorination; photocatalytic oxidation, holes, $^{\bullet}$OH radicals*

1. INTRODUCTION

The attractive properties of titanium dioxide as photocatalyst have been thoroughly investigated in the last decades.[1] Among the different features affecting photoactivity, surface properties obviously exert a dominant influence,[2] reactant adsorption and electron transfer at the interface between the solid and the reactant-containing medium being fundamental steps in photocatalytic processes.[3] Moreover, the photoactivity of the solid surface vary depending on the exposed crystal facets.[4]

As to anatase, regarded as the most photocatalytically active titania polymorph,[5,6] the {101} and {001} facets differ in surface energy, number of undercoordinated Ti atoms and position of the conduction and/or valence band edge.[7,8] Since Yang *et al.*[9] first succeeded in increasing the abundance of high-energy {001} facets by changing their relative stability with respect to {101} ones, several attempts have been made of tailoring the anatase crystal shape[10] and understanding how the photocatalytic activity is affected by the surface composition in terms of exposed facets. The performance of shape-controlled anatase has been tested in a number of photocatalytic reactions of environmental interest, *e.g.* Cr(VI) reduction,[11–13] ammonia oxidation[14] and the degradation of several organic pollutants.[15,16] Yet, no general conclusion has been drawn about either the photoactivity order of anatase crystal facets or their optimal balance, since different reports provided contradictory results.[17–21] This is partly due to the great variety of employed test reactions, involving different substrates adsorbed onto the photocatalyst from the liquid or the gas phase and undergoing oxidative or reductive transformations. Furthermore, the specific role of crystal facets needs to be clearly distinguished from other simultaneous contributions to photoactivity, related to the adopted shape control strategy. This is the case of capping agents, commonly employed to preferentially stabilize the {001} facets during the crystal growth,[7,22,23] that are difficult to be

completely removed from the photocatalyst surface[24,25] and may influence the adsorption of reactants to an extent depending on their residual amount.

The present work is focused on evaluating the efficiency towards organics photooxidation of a series of anatase samples prepared *via* a hydrothermal route in the presence of different amounts of HF, added as a capping agent to modulate the ratio of {001} to {101} facets. By systematically comparing the intrinsic structural features of the prepared materials with their photoactivity before and after calcination, performed to remove residual fluorine from the anatase surface,[18,19,26] we were able to highlight the role of the amount of exposed {001} facets among a series of concurrent effects related to specific surface area, surface fluorination and organization of anatase crystals into aggregates.

In choosing the photocatalytic test reactions we tried to avoid those in which specific factors, other than the intrinsic performance of the photocatalyst, influence the output of the experiment. This occurs, for example, when organic dyes are chosen as test substrates,[27–30] because they may undergo self-sensitized degradation or be photocatalytically decomposed through either oxidative or reductive paths. Therefore we selected a test reaction based on a transparent substrate, which provides evidence of the inherent oxidative ability of photocatalytic materials, *i.e.* formic acid photomineralization in aqueous suspension.[31] Indeed, this model organic substrate is converted into CO_2 through its direct oxidation by photogenerated valence band holes,[32] with no stable intermediates formation, thus allowing a straightforward assessment of photoactivity.[33] The synthesized anatase photocatalysts were also tested in the oxidation of another transparent substrate, *i.e.* in terephthalic acid conversion into 2-hydroxyterephthalic acid,[34–36] which is largely employed as a selective test of $^{\bullet}OH$ radical-mediated photocatalytic oxidation.

2. EXPERIMENTAL SECTION

2.1. Photocatalysts preparation. A series of photocatalysts, denoted as HT series, was synthesized through a hydrothermal route.[37] A fixed amount of titanium isopropoxide (5 mL) was mixed under stirring for 15 min in a Teflon liner with different volumes of a 48 wt.% HF solution and different amounts of water (see Table S1 in the Supporting Information) up to a 5.6 mL final volume. Only in the case of the highest content of fluorine the final volume was larger, *i.e.* 6.2 mL. A reference sample was prepared under the same conditions by simply adding 0.6 mL of water (and no HF) to titanium isopropoxide. The liner was then transferred into a stainless-steel autoclave, which was closed and heated at 180 °C in an electric oven for 24 h. Once cooled down naturally to room temperature, the precipitate was washed several times with water, until the fluoride ion concentration, determined by ion chromatography with conductivity detection (Metrohm 761 Compact IC), was below 5 ppm. The precipitate was then collected, dried at 70 °C overnight and ground into a fine powder in an agate mortar. The so-obtained materials were labeled as HT_X, where HT refers to the employed hydrothermal preparation method, while X stands for the nominal F/Ti molar ratio, ranging from 0 to 2.0.

In order to optimize the method for surface fluorine removal, the HT_1 sample was either calcined at different temperatures, *i.e.* 400, 500 and 600 °C, or washed with a 0.1 M NaOH solution. As detailed in the Supporting Information, the best photoactivity result in formic acid photodegradation was attained after annealing at 500 °C (see Table S2). The relatively poorer result obtained after washing HT_1 with NaOH is probably due to the presence of residual surface sodium (4.3 at.%) on TiO_2, detected by XPS measurements.[38] Therefore, a portion of all samples of the HT series was calcined in air at 500 °C for 2 h to remove surface fluorine[39] and the so obtained photocatalysts were labeled HT_500_X.

All reagents were purchased from Aldrich and employed as received. Water purified by a Milli-Q water system (Millipore) was used throughout.

2.2. Characterization. X-ray powder diffraction (XRPD) patterns were collected on a Panalytical X'Pert Pro diffractometer, using Ni-filtered Cu K_α radiation, at a scan rate of 0.05 degree s^{-1}. Structural and line profile analysis was performed by means of the GSAS software[40] by fitting XRD lines using a modified Pseudo-Voigt function.[41] Instead of using the Scherrer formula, often employed to determine the particle size by the fit of a single Bragg reflection,[12,20,42,43] the line profile analysis from Rietveld refinements was employed, which takes into account all the reflections of the diffraction pattern, thus allowing the contribution of the particle size to be discerned from that of the lattice strain.[44]

In this framework, crystal shape anisotropy is described by means of two parameters (p_1 and p_2) accounting for *hkl*-dependent reflection broadening, from which average values of the crystal width (w) and thickness (t) were calculated, as follows:[45]

$$w = \frac{K \cdot \lambda}{p_1} \tag{1}$$

$$t = \frac{K \cdot \lambda}{p_2} \tag{2}$$

where K is the Scherrer constant, which was set to 0.9, and λ is the incident radiation wavelength (in nm). Since K and p are dimensionless, the unit of the size is the same as the unit of the wavelength. Further details can be found in ref. 44.

Hence the percent amount of {001} facets, %{001}, was calculated from the surface area of the {001} and {101} facets, $S_{\{001\}}$ and $S_{\{101\}}$, respectively, according to geometrical considerations (see Figure 1) using the following formula:

$$\%\{001\} = \frac{S_{\{001\}}}{S_{\{001\}} + S_{\{101\}}} \cdot 100 \tag{3}$$

with

$$S_{\{001\}} = 2\left(w - t\cot\varphi\right)^2 \tag{4}$$

$$S_{\{101\}} = \frac{2t}{\text{sen}\,\varphi}\left(2w - t\cot\varphi\right) \quad (5)$$

where φ is the angle between the {001} and {101} facets. Its value was set to 68.3°, which corresponds to the theoretical angle between the (001) and (101) lattice planes of anatase.

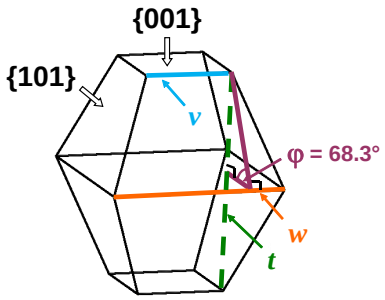

Figure 1. Geometrical model of anatase single crystal: crystal width (*w*) and thickness (*t*) are indicated together with the angle (φ) between the {001} and {101} crystal facets and the minor base (*v*) of the trapezoidal {101} facets.

Raman spectra were acquired with a ThermoFisher DXR Raman microscope, using a 532 nm laser (5.0 mW) focused on the sample with a 50× objective (Olympus) to obtain a *ca.* 1 μm spot size. The average values of at least 4 measurements performed on different spots were considered.

Field-emission scanning electron microscopy (FE-SEM) images were collected by using a Zeiss SUPRA® 40 scanning electron microscope, operating at a 5-7 kV accelerating voltage, at a 3-4 mm working distance. Samples, previously sonicated in isopropanol, were dropped on a silicon wafer and dried prior to measurements.

HR-TEM analyses were carried out with a Zeiss Libra 200 electron microscope operating at 200 kV. Finely ground samples were dispersed in isopropanol, in an ultrasonic bath. A drop of the suspension was gently deposited on a holey-carbon film supported on a copper grid. After solvent evaporation, micrographs were taken spanning wide regions of all examined samples, in order to provide a truly representative statistical map of the powders.

Nitrogen adsorption/desorption data were collected at 77 K using a Micromeritics Tristar II 3020 V1.03 apparatus, after outgassing at 300 °C for 1 h under a N_2 stream. Specific surface area (SSA) values and pore size distribution were obtained by applying the Brunauer−Emmett−Teller (BET) and the Barret−Joyner−Halenda (BJH) method, respectively, to the adsorption isotherms.

X-ray photoemission spectroscopy (XPS) data were collected in a multi-technique ultra-high-vacuum (UHV) chamber (base pressure: 1.0×10^{-9} mbar) equipped with a VG MKII ESCALAB electron analyzer (5 channeltrons). Measurements were made at room temperature in normal emission using a non monochromatized Mg anode X-ray source ($h\nu$ = 1253.6 eV). Powder samples were suspended in bi-distilled water and drop-casted on high-purity copper foils. After drying in air, the obtained films were introduced into the UHV chamber and outgassed overnight. The charging observed during measurements was corrected by aligning the Ti $2p_{3/2}$ core-level peak signal to 459.0 eV.

Diffuse reflectance (DR) spectra of the photocatalyst powders were recorded on a Jasco V-670 spectrophotometer equipped with a PIN-757 integrating sphere, using PTFE as a reference, and then converted into absorption (*Abs*) spectra ($Abs = 1 - R$).

2.3. Formic acid photocatalytic oxidation. All formic acid (FA) photocatalytic degradation runs were performed under atmospheric conditions using the already described photoreactor and setup,[46] including an Osram Powerstar 150 W lamp as irradiation source, emitting ultraviolet and visible light at $\lambda > 340$ nm, mounted on an optical bench. The light intensity on the reactor in the 300 - 400 nm range was 5×10^{-8} Einstein s^{-1}, as calculated from the emission spectrum of the lamp and its full emission intensity, which was regularly checked with an optical power meter. The irradiated aqueous suspensions always contained 0.1 g L^{-1} of photocatalyst and a FA initial concentration equal to 1.0×10^{-3} mol L^{-1}. The adsorption equilibrium of the substrate on the photocatalyst surface was attained under

magnetic stirring, before starting irradiation. Stirring was continued during the photocatalytic runs. Portions (3 mL) of the suspension were withdrawn from the photoreactor at different time intervals during the runs and centrifuged employing an EBA-20 Hettich centrifuge. The supernatant was analyzed for residual FA content by ion chromatography with conductivity detection, employing a Metrohm 761 Compact IC instrument, after calibration for formate ion concentration in the 0−50 ppm range. All kinetic runs were performed up to ca. 70% substrate degradation, and repeated at least twice, to check their reproducibility.

2.4. Terephthalic acid photocatalytic oxidation. The same photoreactor and setup were employed to test the efficiency of the photocatalysts in terephthalic acid oxidation, but a different procedure was followed.[47] For each photocatalytic run 10 mg of photocatalyst were first dispersed in 45 mL of ultrapure water by means of 30-min long sonication. Then a 5 mL aliquot of a 5×10^{-3} M terephthalic acid solution in 2×10^{-2} M NaOH was added and the suspension was left under stirring in the dark for 30 min, in order to allow substrate adsorption on the catalyst surface, prior to irradiation under stirring. Portions of the suspension collected at fixed time intervals were centrifuged and the concentration of the fluorescent reaction product was determined in the supernatant. Emission spectra (λ_{exc} = 315 nm, λ_{em} = 425 nm) were recorded on an Edinburgh FLS980 spectrofluorimeter, after calibration.

3. RESULTS AND DISCUSSION

3.1. Phase composition and morphological features. As shown in Figure 2, all samples match the standard anatase XRPD pattern and no characteristic peaks of other TiO_2 polymorphs such as rutile and brookite are observed. In addition, the (100) and (110) peaks of the cubic $TiOF_2$ phase are clearly observed in the pattern of sample HT_2 at $2\theta = 23°$ and 33°, respectively (see inset (a) in Figure 2). The $TiOF_2$ amount in HT_2 was around 4 wt.%. A smaller amount of $TiOF_2$ (around 0.3 wt.%) was determined also in sample HT_1 through

Rietveld refinement. On the other hand, all samples belonging to the HT_500 series consist of pure anatase, without any evidence of $TiOF_2$ (see Figure S1).

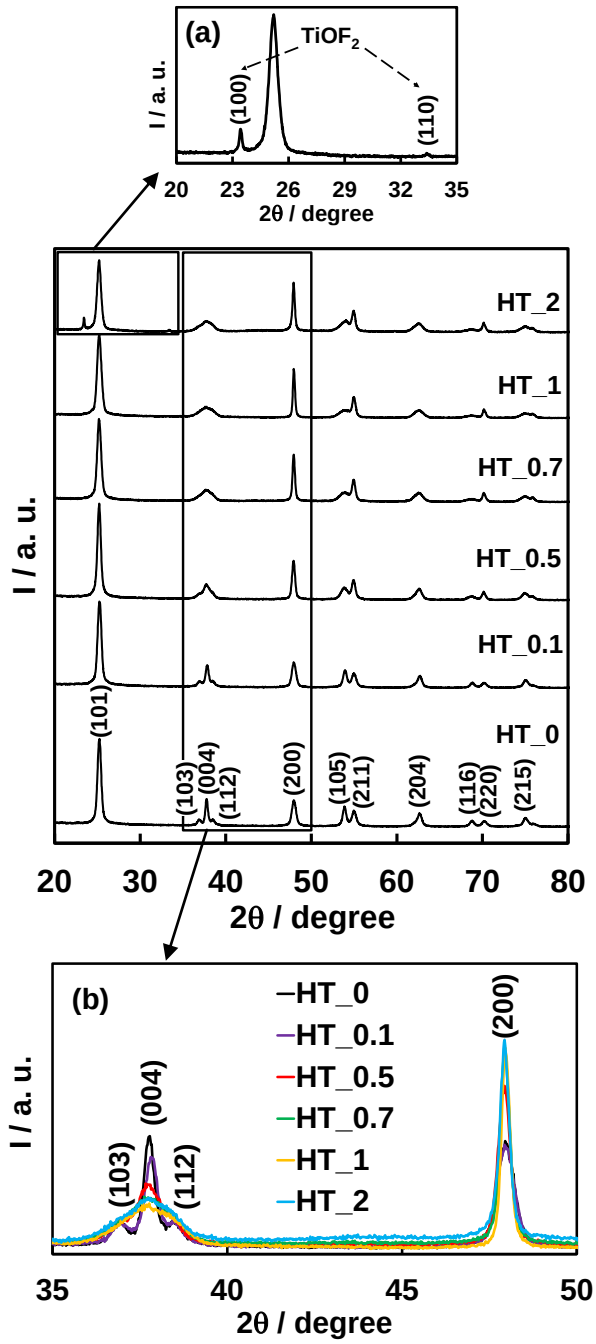

Figure 2. XRPD patterns of the HT series; inset (a) displays an enlarged portion of the HT_2 sample pattern, showing the presence of the $TiOF_2$ phase; inset (b) shows the overlapped HT series patterns in the 35° – 50° 2θ range, evidencing (103), (004), (112) and (200) anatase reflections.

The evolution with the F/Ti ratio of anatase *a* and *c* lattice parameters (*i.e.* the shorter and the longer lattice parameter in the tetragonal cell of anatase, respectively, see Figure S2 in the Supporting Information) evidences a clear discontinuity in passing from F/Ti = 0.1 to 0.5: for lower fluorine contents *a* increases and *c* decreases as F/Ti is increased, while for fluorine-rich materials the reverse is obtained. As for the HT series, the value of *c* increases up to F/Ti = 0.7 reaching a sort of plateau for higher F/Ti values (Figure S2b), which is accompanied by the separation of the $TiOF_2$ phase.

The above findings support progressive insertion of F into the anatase lattice for $0 \leq F/Ti \leq 0.7$, while for F/Ti values larger than 0.7 no more fluorine should be incorporated into anatase, but it rather segregates into the $TiOF_2$ crystalline phase, that was actually detected in HT_1 and, especially, HT_2. The formation of $TiOF_2$ may reduce the amount of fluorine in TiO_2, the cell parameter values for HT_2 being between those obtained for HT_0.5 and HT_0.7. Nevertheless, the crystallite size, especially in the case of crystallites smaller than 10 nm, may also significantly affect the actual value of lattice parameters.[48,49]

Specific trends of *a* and *c* parameters can hardly be identified for calcined samples (HT_500 series in Figure S2). In this case the behavior of *c* is similar to that of as-prepared samples, though its relative variation is smaller and no plateau effect is observed for high F/Ti values. Both effects can be ascribed to the lower residual fluorine amount after annealing.

The increase of fluorine amount has a clear impact on the experimental XRPD patterns of the HT series in the 35° - 50° 2θ range (see inset b of Figure 2). In particular, reflections with a marked *h* component (*e.g.* (200)) shrink with increasing F/Ti ratio, while those with ($l > h$, k) show the opposite behavior. This is due to progressive morphological changes which can be appreciated by comparing the percent amounts of {001} facets reported in Table 1, calculated according to equation (3).

As shown in Figure 3, for the HT series the percentage of exposed {001} facets increases with increasing the fluorine content up to F/Ti = 1 and then decreases, whereas a sort of plateau seems to be reached for the HT_500 series at F/Ti ≥ 0.7.

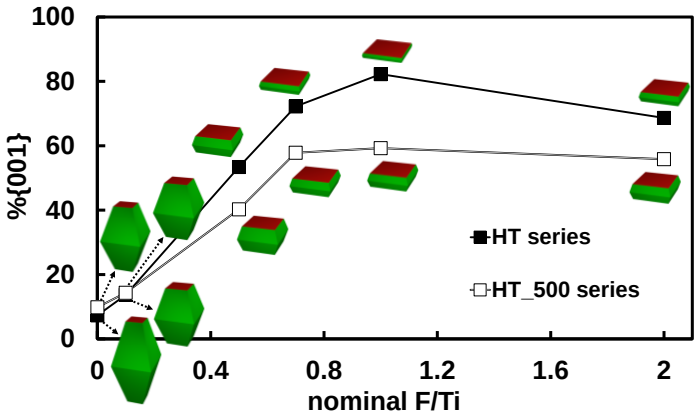

Figure 3. Percent exposed {001} facets obtained from XRPD analysis for the HT (full squares) and HT_500 (open squares) photocatalysts series as a function of the F/Ti ratio; the crystal shape expected on the basis of the calculated percentage of {001} facets is shown for each sample. Estimated standard deviations are covered by data markers.

Calcination at 500 °C causes a general decrease of the {001} facets percent amount (Table 1 and Figure 3), thus determining a smaller degree of truncation, except for HT_0 and HT_0.1, where no significant variation is observed upon calcination. Therefore annealing reduces the degree of truncation of anatase crystals, *i.e.* the *v* to *w* ratio (see Figure 1), thus converting the original plate-like shape of nanocrystals to a more isotropic one.

Besides through XRPD analysis, the percentage of {001} facets was also calculated according to a recently proposed alternative approach based on Raman spectroscopy,[50] as the intensity ratio of the A_{1g} peak (514 cm^{-1}) to the E_g peak (144 cm^{-1}) of anatase. These peaks are that associated to the antisymmetric bending vibration mode (A_{1g}) of O-Ti-O groups, the intensity of which increases with the amount of {001} facets, and that arising from the symmetric stretching vibration modes (E_g), decreasing accordingly. Examples of normalized

Raman spectra obtained with HT_0.1 and HT_1 are shown in Figure S3. The percent amounts of {001} facets of our samples calculated by this approach are shown in Figure S4 in comparison with those obtained by XRPD analysis.

Table 1. Crystal size, percent amount of exposed {001} facets and atomic percent amount of surface fluorine for the HT and HT_500 photocatalysts series.

sample	width (w)[a] / nm	thickness (t)[a] / nm	% {001}[b]	% F[c]
HT_0	21.7±0.2	31.7±0.9	7.3±0.6	-
HT_0.1	22.3±0.2	25.3±0.6	13.7±0.7	4.0
HT_0.5	41.8±0.4	13.72±0.12	53.4±0.6	3.6
HT_0.7	61.1±1.3	9.88±0.11	72.2±0.9	5.0
HT_1	91±2	8.64±0.09	82.3±0.8	6.5
HT_2	53.2±1.3	10.03±0.15	68.7±1.2	n.a.
HT_500_0	23.6±0.2	31.1±0.6	9.8±0.5	-
HT_500_0.1	22.6±0.2	25.0±0.4	14.3±0.5	1.6
HT_500_0.5	39.5±0.4	19.5±0.2	40.2±0.6	3.0
HT_500_0.7	59.7±0.7	16.9±0.2	57.8±0.7	2.2
HT_500_1	67.1±0.9	18.0±0.2	59.3±0.8	1.8
HT_500_2	59.4±0.8	18.0±0.2	55.8±0.8	n.a.

[a] Obtained from XRPD measurements.

[b] Calculated from crystal sizes by assuming a truncated square-bipyramidal shape of anatase crystals with the angle between (001) and (101) planes fixed at 68.3 °.

[c] Obtained from the 684.5 eV XPS peak.

The results obtained from Raman measurements confirm the trend obtained from XRPD data for both HT and HT_500 photocatalysts series, with the percent amount of {001} facets increasing with increasing F/Ti ratio, and are in quite satisfactory agreement for low F/Ti ratios. However, Raman spectroscopy analysis tends to significantly underestimate the percent amount of {001} facets in plate-like crystals, at relatively high F/Ti ratios (Figure S4). By taking into account that the percentage of {001} facets for anatase crystals grown in an acidic-neutral environment without any specific capping agent is predicted to be around 3-4%,[51] we observe that for HT_0, synthesized under such conditions, the percent amount of {001} facets determined by the XRPD method is closer to this value than that obtained from Raman measurements. This points to XRPD as a more reliable method for percent facets estimation.

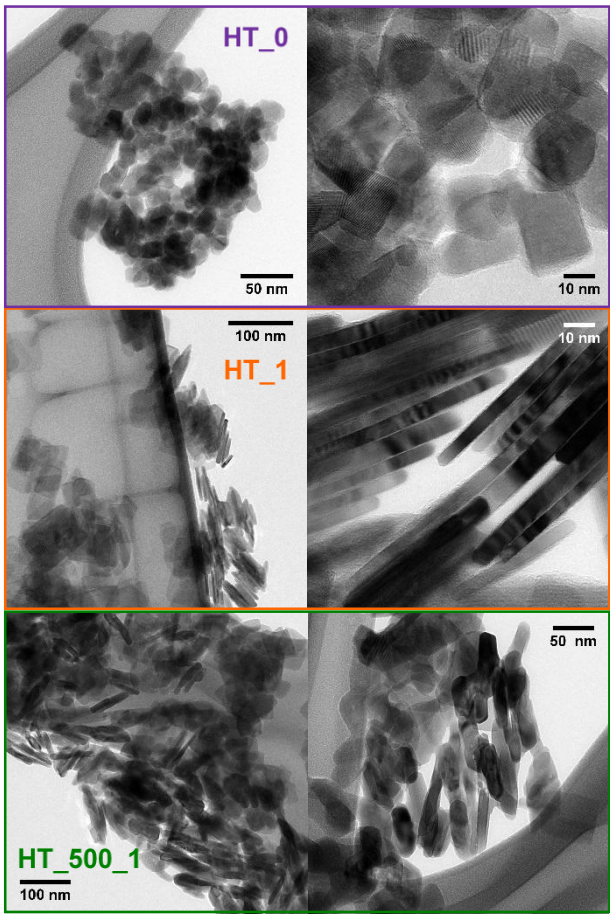

Figure 4. HR-TEM images of HT_0, HT_1 and HT_500_1.

The morphological effects due to the use of HF as capping agent can be appreciated by comparing the HR-TEM images obtained for HT_1 with those of reference HT_0. As shown in Figure 4, HT_1 is incontrovertibly formed by plate-like crystals, the surface of which is dominated by {001} facets. Their regular shape produces ordered aggregates, in which crystals are piled up face-to-face, one above the other, thus minimizing the total surface energy.[52] Consequently a large portion of theoretically available {001} surface seems to be practically inaccessible to substrate adsorption. On the contrary, the casual distribution of particles displayed by HT_0 aggregates (Figure 4) is coherent with an isotropic shape of crystals.

On the other hand, the effects induced by the heat treatment here chosen to remove surface fluorine clearly emerge by comparing the HR-TEM images of HT_1 and HT_500_1 in Figure 4. A plate-like morphology can still be recognized in HT_500_1, though the shape of the crystals appears quite irregular, leading to a more disordered array, with respect to HT_1 crystals. The resulting structure of the aggregates seems to increase the exposure of {001} facets, making them more available for substrate adsorption than before calcination. Furthermore, as shown by both X-ray diffraction data and HR-TEM analysis, the crystal size markedly increases along the [001] direction upon heat treatment, though slightly decreasing along the [100] direction, probably due to surface energy minimization, as is the case of crystal packing into piles observed for HT_1 (Figure 4).

The FE-SEM images of calcined samples shown in Figure 5 evidence an increase in the side length of crystals with increasing F/Ti ratio, as well as a corresponding decrease in thickness, in agreement with XRPD findings. Crystal width values span from *ca*. 20 (for HT_500_0.1) to *ca*. 80 nm (for HT_500_1), while thickness ranges from *ca*. 30 to *ca*. 7 nm as the F/Ti ratio increases. Thus the general morphological evolution, from almost isotropic to plate-like crystals, evidenced by XRPD analysis for the HT series is substantially retained

after the thermal treatment. However, after calcination the crystals are more irregular in shape and this tendency is maximum for HT_500_2, for which the platelet-like geometry can hardly be recognized (Figure 5). This could be related to the removal of a high amount of fluorine during the thermal treatment, which also causes the disappearance of $TiOF_2$ evidenced by phase composition analysis.

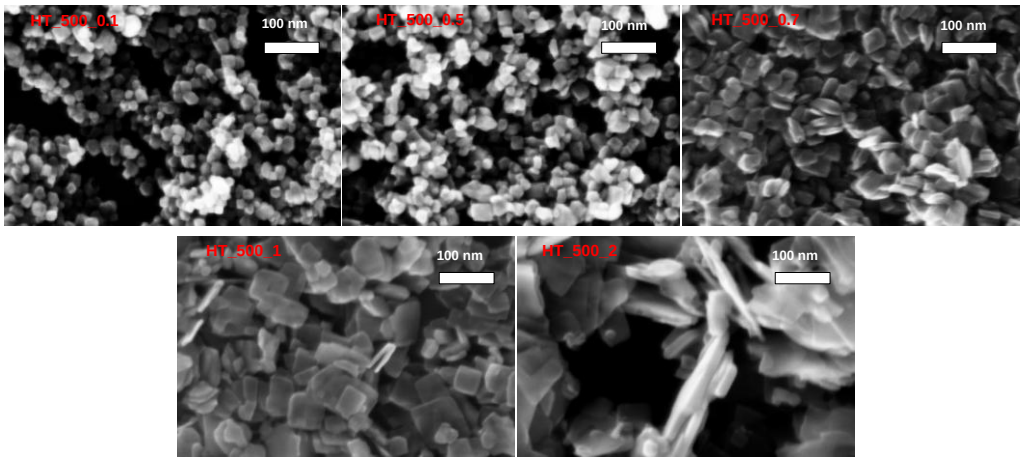

Figure 5. FE-SEM images of fluorine-containing samples of the HT_500 series; the dimension bar corresponds to a 100 nm distance for all images.

3.2. Surface and optical properties. The SSA values obtained for the HT and HT_500 photocatalysts series are reported in Table 2. Samples belonging to the HT series exhibit similar SSA, possibly increasing with increasing the F content, from 80 m^2 g^{-1} for F/Ti = 0 to 92 m^2 g^{-1} for F/Ti = 1.0, while no variation can be appreciated within the HT_500 series, all SSA values of the $0 \leq F/Ti \leq 1$ samples being in the 50 – 59 m^2 g^{-1} range. As expected, calcination provokes a general decrease in SSA due to crystallites sintering. Both F/Ti = 2.0 samples in the two series have a SSA markedly lower than those of the other samples in the same series.

Representative N_2 adsorption/desorption isotherms collected for samples belonging to both series are reported in Figure S5. The presence of a characteristic hysteresis loop allows their

classification as type IV isotherms.[53] The observed porosity may originate from the packing of the TiO_2 crystals, since they are not inherently porous.[54] With increasing F/Ti ratio, the hysteresis loops progressively shrink, passing from a H2 type shape, connected to the presence of the so–called "ink bottle" pores, to a H3 type shape, usually observed with aggregates of plate-like particles giving rise to slit-shaped pores.

Table 2. Specific surface area of photocatalysts belonging to the HT and HT_500 series.

F/Ti molar ratio	SSA / m^2 g^{-1}	
	HT series	HT_500 series
0	80.0 ± 0.6	54.9 ± 0.7
0.1	81.4 ± 0.9	59.0 ± 0.8
0.5	84.3 ± 1.0	49.3 ± 0.2
0.7	92.7 ± 0.7	57.2 ± 0.8
1	92.3 ± 0.9	55.5 ± 0.5
2	59.9 ± 1.0	33.8 ± 0.4

Furthermore, for both photocatalysts series the hysteresis loops shift to higher relative pressures with increasing F/Ti ratio, indicating a progressive pore enlargement. The same kind of shift of the hysteresis loop was observed for all samples upon calcination, indicating pore enlargement as well. This can be better appreciated from the shift to larger pore diameters of the pore size distribution maximum observed after the thermal treatment (see Figure 6a, showing results obtained with HT_0.7 as a representative sample).

Moreover, the pore size distribution for the HT_500 series reported in Figure 6b shows similar narrow unimodal distributions which gradually shift toward larger pore diameters with increasing F/Ti ratio up to 0.7. A markedly different distribution (broader and peaking at

larger pore diameters) is obtained for HT_500_1. This indicates a progressive growth in pore size as the crystals approach the plate-like shape, and also a unique crystal packing for HT_500_1. Such a peculiarity especially emerges in the comparison with HT_500_0.7, characterized by a similar percentage of {001} facets. This suggests that the packing observed after calcination strictly depends on the different shapes of the crystals before annealing. Thus, an increase of F/Ti ratio promotes the formation of less compact aggregates, containing larger pores, which become even larger after calcination, in agreement with TEM and FE-SEM images.

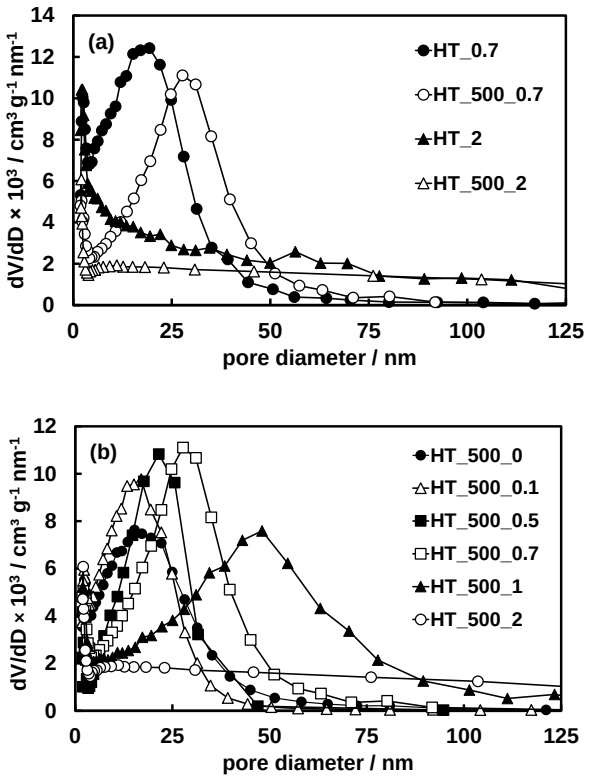

Figure 6. (a) Pore size distribution for samples with F/Ti = 0.7 and 2.0, before and after calcination; (b) pore size distribution for the HT_500 photocatalysts series.

Interestingly, only HT_2 and HT_500_2 display no hysteresis in isotherm analysis. This may be attributed to the presence of macropores, consistently with the FE-SEM images of

HT_500_2 (Figure 5) and also with the peculiarly broad pore size distribution of both samples shown in Figure 6a.

The surface composition of the anatase materials was assessed through XPS analysis. First of all, almost identical Ti 2p doublet signals, with the two components at binding energy (BE) 464.7 and 459.0 eV, assigned to Ti $2p_{1/2}$ and Ti $2p_{3/2}$, respectively, were recorded with all samples. At the same time similar O 1s spectra were obtained with all samples, showing a main peak centered at 530.2 eV, typical of oxygen in the TiO_2 lattice, and a shoulder at higher BE (531.6 eV), assigned to surface hydroxyl groups.[55]

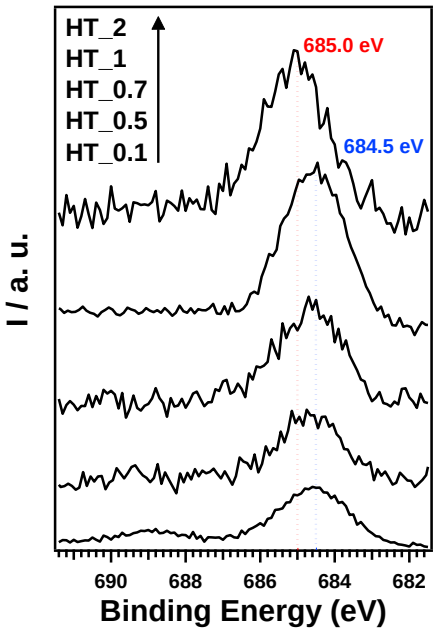

Figure 7. XPS spectra in the F 1s region of the HT series samples; the shift of the peak maximum for HT_2 with respect to the other samples is highlighted.

Concerning the F1s XPS region, the spectra obtained with the HT series are shown in Figure 7. An asymmetric peak centered at about 684.5 eV, arising from terminal Ti-F bonds,[56] was detected for all samples, indicating the presence of surface fluorine. This signal is known to result from the combination of two different components, which can be resolved by a deconvolution procedure (see Figure S6).[57] The main one, centered at 684.3 eV, is generated

by fluorine atoms replacing only one of the two -OH groups coordinated to a surface Ti atom and the minor one, at 685.3 eV, derives from fluorine atoms coordinated together to the same Ti center. Notably, the XPS peak maximum for HT_2 is shifted to higher BE with respect to the other samples, in line with the presence of the crystalline $TiOF_2$ phase [58,59] detected in this sample.

Another XPS peak at 688.8 eV, usually attributed to substitutional lattice fluorine ions,[60] could be identified only in the case of HT_0.1 (see Figure S6) and HT_500_0.1. However the presence of lattice fluorine also in other samples cannot be ruled out, possibly being below the detection limit of the XPS technique.[57]

As shown in Table 1, the amount of surface fluorine detected by XPS analysis slightly increases with increasing F/Ti ratio in the HT series, while a significantly lower, quite uniform F-coverage was detected in the HT_500 series (except for HT_500_0.5).

The DR spectra of the photocatalysts (see Figure S7) show the usual absorption onset of anatase at $\lambda < 400$ nm, with samples synthesized in the presence of the fluorine capping agent possibly exhibiting a slightly blue-shifted absorption edge. A similar,[61] as well as the opposite behavior[18,22,47] have been reported in the literature with an open debate about the dependence of the anatase band gap on facet composition. The different crystal size, which significantly affects the band gap, could be responsible for the observed discrepancies, even more than the percentage of exposed {001} facets.[39] Anyway, recent theoretical and experimental work[26,62] indicate that the band gap should not depend on the amount of exposed specific facets.

Finally, the heat treatment at 500 °C eliminates the low, almost uniform absorption contribution extending over the whole visible range, possibly originated from residual surface carbon after the synthesis (see HT_1 *vs.* HT_500_1 spectra in Figures8.

3.3. Photocatalytic oxidation of formic acid. The photocatalytic degradation of FA occurred at constant rate, *i.e.* according to a zeroth-order rate law, as in previous studies.[32,63,64]

Therefore the activity of the here investigated TiO_2 materials in FA photocatalytic oxidation can be compared in terms of zeroth-order rate constants *k*, which were normalized for the photocatalysts' surface area, to better extract their intrinsic photoactivity. Surface normalized rate constants of FA photocatalytic oxidation obtained employing the photocatalysts with a nominal F/Ti ratio ranging from 0 to 1 are reported in Figure 8, together with the residual surface fluorine percent amount detected on their surface by XPS analysis.

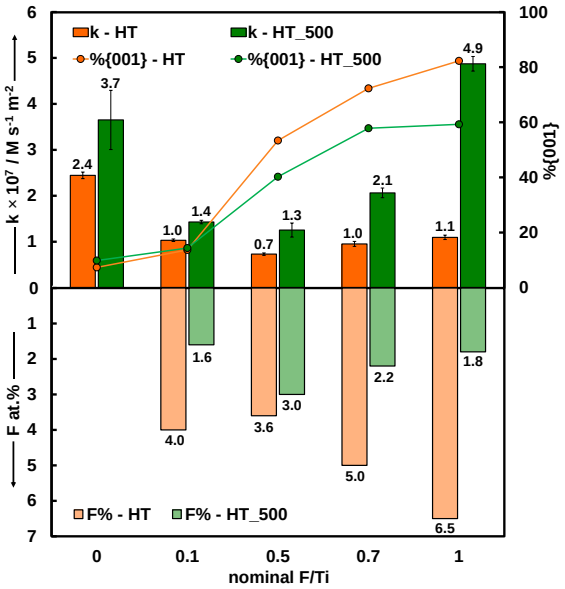

Figure 8. Surface normalized rate constants of FA photomineralization (filled columns in the upper panel) and percent surface fluorine amount detected by XPS analysis (patterned columns in the lower panel, in reverse axis scale) along with percentages of {001} facets obtained from XRPD analysis (circles, upper panel) for both HT and HT_500 series.

First of all, the photoactivity of fluorine-containing samples of the HT series are relatively low and do not exhibit any trend with the nominal F/Ti ratio, as already reported for as-prepared fluorine-containing photocatalysts.[18] Reference HT_0 clearly displayed superior photocatalytic activity among HT series photocatalysts. After heat treatment at 500 °C all photocatalysts show higher photoactivity. In particular, HT_500_1 is by far the best photocatalyst, exhibiting an activity similar to that of benchmark P25 TiO_2 from Evonik [$k = (4.76 \pm 0.15) \times 10^{-7}$ M s^{-1} m^{-2}] and better than that of reference sample HT_500_0. Moreover,

an overall photoactivity increase can be clearly appreciated with increasing the {001} facet percentage for F-containing samples (Figure 8).

The general improvement in photoactivity observed upon calcination can be ascribed to different effects brought about by the thermal treatment. Firstly, the partial removal of surface fluorine (together with other adsorbed species), proved by XPS analysis, certainly contributes in increasing the photoactivity in this specific test reaction. In fact residual fluorine is expected to inhibit the adsorption of FA, thus preventing its degradation, which occurs through direct oxidation on the TiO_2 surface.[32] Moreover, the F-terminated surface, displaying a lower amount of surface –OH groups, is less efficient in creating ≡Ti-O$^{\bullet}$ effective traps for photogenerated valence band holes, according to the following reaction:[65]

$$\equiv\text{Ti-OH} + h_{VB}^{+} \rightarrow \equiv\text{Ti-O}^{\bullet} + \text{H}^{+} \quad (6)$$

but it rather produces free $^{\bullet}$OH radicals as oxidizing species:

$$\equiv\text{Ti-F} + h_{VB}^{+} + \text{H}_2\text{O} \rightarrow \equiv\text{Ti-F} + {}^{\bullet}\text{OH} + \text{H}^{+} \quad (7)$$

Calcination is also expected to increase the photocatalytic activity as a consequence of the increased crystallinity of the material and also of the formation of beneficial surface trapping sites for charge carriers,[66] when fluorine is removed from the titania surface.

All these factors contribute to the general photoactivity improvement displayed by all photocatalysts upon calcination, irrespective of their crystal morphology. However, by carefully considering how photoactivity varies within the HT_500 series, a clear contribution of crystal shape can be recognized, regardless of fluorine removal. In fact, for similar amounts of residual surface fluorine, the photocatalytic activity of plate-like HT_500_1 is far higher than that of the slightly truncated HT_500_0.1. Furthermore, HT_500_0.5 and HT_500_0.7, featuring a considerable percentage of {001} facets, show comparable and better performances, respectively, than HT_500_0.1, though bearing larger amounts of fluorine on their surface (Table 1).

Thus, the superior activity of the {001} facets is fully revealed only upon calcination, inducing not only surface fluorine removal, but also favorable changes in crystal morphology. In fact, as-prepared crystals with large F/Ti ratios are regularly-shaped nanosheets, piled in an ordered face-to-face fashion (Figure 4). Under such conditions, a significant percentage of {001} facets is not available to FA adsorption. On the contrary, a beneficial rearrangement in the crystal packing is favored by their irregular shape after calcination at 500 °C, though they still retain the desired platelet-like morphology, as clearly shown by electron microscopy images (Figure 4 and 5) as well as by XRPD analysis (Table 1). Therefore, even if the degree of truncation of TiO_2 nanocrystals decreases upon calcination, the morphology changes may result in an increase of the actually exposed {001} surface, allowing for adsorption (and thus faster degradation) of FA.

Such changes are reflected in the porosity of the materials after calcination. Its relevant contribution to photoactivity has been fully evidenced here for the first time and appears to depend on the original morphology of the crystals. In fact, among calcined samples, HT_500_1 seems to particularly benefit from a favorable crystal aggregation, since its photoactivity markedly differs from that of HT_500_0.7, though the two samples bear similar percent amounts of {001} facets. This finding is supported by the unique porosity profile characterizing only HT_500_1 among all HT_500 series samples (Figure 6b) that, along with the highest percentage of {001} facets and lowest amount of surface fluorine, makes it the best performing photocatalyst.

The improved photocatalytic activity might not be simply ascribed to a larger amount of {001} facets, but may result from an appropriate interplay between different facets.[10,11] Indeed, it has been reported that {001} and {101} facets differ in the location of their band edges, so that electrons preferably migrate to {101} facets, while holes tend to move to {001} facets.[26,35] Thus, the coexistence of such facets in a proper balance allows spatial separation of

photogenerated charges and thus higher photoactivity. Notably, the percent amount of {001} facets in most efficient HT_500_1 in FA degradation (59%) is very similar to that recently found to be optimal to hinder the undesired electron-hole recombination (55%).[26]

3.4. Photocatalytic oxidation of terephthalic acid. The conversion of terephthalic acid (TA) into 2-hydroxyterephthalic acid (TAOH) was employed to investigate how anatase morphology in better performing HT_500 photocatalysts with a similar surface residual fluorine amount (1.8 ± 0.2 at.%) influences the photocatalytic production of hydroxyl radicals from water molecules oxidation. The so produced hydroxyl radicals then attack organic substrates through the so called indirect oxidation mechanism.

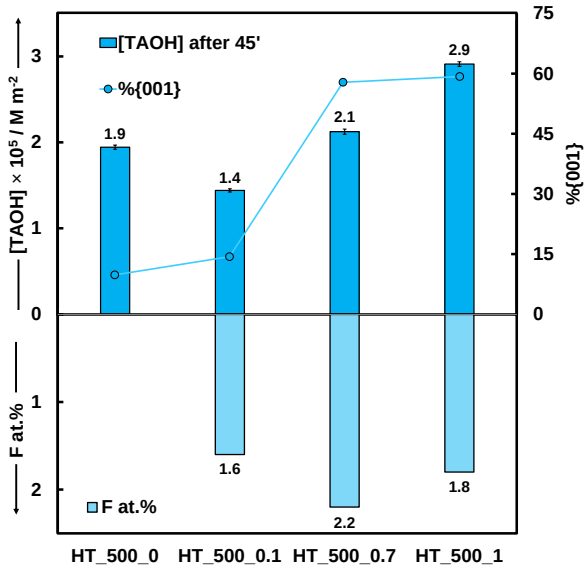

Figure 9. Concentration of TAOH per photocatalyst unit surface area after 45 min irradiation (filled columns in the upper panel) and percent surface fluorine amount detected by XPS analysis (patterned columns in the lower panel, in reverse axis scale) along with dispersion plots (upper panel) of the percentage of {001} facets obtained from XRPD for selected samples of the HT_500 series.

The amount of photogenerated $^{\bullet}$OH radicals, trapped in the form of fluorescent TAOH, was found to increase during irradiation of the photocatalyst suspensions, as shown in Figure S8. TAOH concentrations detected in the irradiated suspension after 45 min-long irradiation,

normalized with respect to the surface area of each photocatalyst, are compared in Figure 9 together with the residual percent amount of surface fluorine species detected by XPS analysis in HT_500 samples. The photoactivity scale observed for FA mineralization was found to be substantially retained in this reaction too. Also HT_500_0.7, besides HT_500_1, proved to be better than fluorine-free HT_500_0.

Thus, the photoefficiency in $^{\bullet}$OH radicals generation is also favored by {001} facets exposure. In this case the influence of residual capping fluorine on both substrate adsorption and $^{\bullet}$OH production (according to equation (7)) should play a minor role, this test reaction proceeding in basic medium, *i.e.* with surface fluorine being displaced by terminal −OH groups.[67,68]

We thus demonstrate that the rate of both direct and $^{\bullet}$OH-mediated photocatalytic oxidation paths is enhanced for anatase with a plate-like morphology, pointing to a superior oxidation ability of {001} facets either alone, or in combination with the most thermodynamically stable {101} facets.

4. CONCLUSIONS

We demonstrate here that the superior photoactivity of {001} facet-enriched anatase TiO_2 is revealed only upon calcination, which not only removes excess residual fluorine that may hinder substrate adsorption, but also triggers morphological changes in crystal aggregates, with a consequent exposure of a larger fraction of {001} facets. Ultimately, the here chosen annealing conditions increase the portion of {001} surface facets effectively available for photocatalytic processes, at the same time essentially preserving the desired plate-like crystal anisotropy. Both direct and $^{\bullet}$OH-mediated photocatalytic oxidation paths are promoted by larger amounts of exposed {001} facets, also possibly coexisting with {101} facets in an appropriate proportion. The best photoactivity in both test reactions was attained by a photocatalyst featuring about 60% of {001} facets.

ASSOCIATED CONTENT

Supporting information. Amounts of employed reagents, preliminary photoactivity tests, XRPD pattern of calcined samples, anatase lattice parameters, Raman spectra, percent amounts of exposed {001} facets according to XRPD and Raman spectroscopy approaches, nitrogen adsorption isotherms, deconvolution of XPS spectra in the F 1s region, UV-vis DR spectra, sample fluorescence spectra of photoproduced TAOH. This material is available free of charge via the Internet at http://pubs.acs.org.

AUTHOR INFORMATION

Corresponding authors

*M. V. Dozzi. E-mail: mariavittoria.dozzi@unimi.it.

*E. Selli. E-mail: elena.selli@unimi.it.

Notes

The authors declare no competing financial interest.

ACKNOWLEDGMENTS

The collaboration of Dr. Mariangela Longhi in collecting nitrogen adsorption isotherms and of Alessio Zuliani in artwork creation are gratefully acknowledged. The use of the instrumentation purchased through the Regione Lombardia – Fondazione Cariplo joint *SmartMatLab* project (Fondazione Cariplo grant 2013-1766) is also acknowledged. This work received support from the Fondazione Cariplo project *Novel Photocatalytic Materials Based on Heterojunctions for Solar Energy Conversion* (grant 2013-0615).

REFERENCES

(1) Hoffmann, M. R.; Martin, S. T.; Choi, W.; Bahnemann, D. W. Environmental Applications of Semiconductor Photocatalysis. *Chem. Rev.* **1995**, *95*, 69−96.

(2) Linsebigler, A. L.; Lu, G.; Yates Jr, J. T. Photocatalysis on TiO_2 Surfaces: Principles, Mechanisms, and Selected Results. *Chem. Rev.* **1995**, *95*, 735−758.

(3) Fox, M. A.; Dulay, M. T. Heterogeneous Photocatalysis. *Chem. Rev.* **1995**, *83*, 341−357.

(4) Diebold, U. The Surface Science of Titanium Dioxide. *Surf. Sci. Rep.* **2003**, *48*, 53−229.

(5) Diebold, U.; Ruzycki, N.; Herman, G. S.; Selloni, A. One Step towards Bridging the Materials Gap: Surface Studies of TiO_2 Anatase. *Catal. Today* **2003**, *85*, 93−100.

(6) Prieto-Mahaney, O.; Murakami, N.; Abe, R.; Ohtani, B. Correlation between Photocatalytic Activities and Structural and Physical Properties of Titanium(IV) Oxide Powders. *Chem. Lett.* **2009**, *38*, 238−39.

(7) Liu, G.; Yang, H. G.; Pan, J.; Yang, Y. Q.; Lu, G. Q.; Cheng, H. Titanium Dioxide Crystals with Tailored Facets. *Chem. Rev.* **2014**, *114*, 9559−9612.

(8) Liu, S.; Yu, J.; Jaroniec, M. Anatase TiO_2 with Dominant High-Energy {001} Facets: Synthesis, Properties, and Applications. *Chem. Mater.* **2011**, *23*, 4085–4093.

(9) Yang, H. G.; Sun, C. H.; Qiao, S. Z.; Zou, J.; Liu, G.; Smith, S. C.; Cheng, H. M.; Lu, G. Q. Anatase TiO_2 Single Crystals with a Large Percentage of Reactive Facets. *Nature* **2008**, *453*, 638–641.

(10) Dozzi, M. V.; Selli, E. Specific Facets-Dominated Anatase TiO_2: Fluorine-Mediated Synthesis and Photoactivity. *Catalysts* **2013**, *3*, 455−485.

(11) He, Z.; Cai, Q.; Wu, M.; Shi, Y.; Fang, H.; Li, L.; Chen, J.; Chen, J.; Song, S. Photocatalytic Reduction of Cr(VI) in an Aqueous Suspension of Surface-Fluorinated Anatase TiO_2 Nanosheets with Exposed {001} Facets. *Ind. Eng. Chem. Res.* **2013**, *52*, 9556−9565.

(12) He, Z.; Jiang, L.; Wang, D.; Qiu, J.; Chen, J.; Song, S. Simultaneous Oxidation of *p*-Chlorophenol and Reduction of Cr(VI) on Fluorinated Anatase TiO_2 Nanosheets with Dominant {001} Facets under Visible Irradiation. *Ind. Eng. Chem. Res.* **2015**, *54*, 808−818.

(13) Yang, Y.; Wang, G.; Deng, Q.; Wang, H.; Zhang, Y.; Ng, D. H. L.; Zhao, H. Enhanced Photocatalytic Activity of Hierarchical Structure TiO_2 Hollow Spheres with Reactive (001) Facets for the Removal of Toxic Heavy Metal Cr(VI). *RSC Adv.* **2014**, *4*, 34577–34583.

(14) Wu, H.; Ma, J.; Li, Y.; Zhang, C.; He, H. Photocatalytic Oxidation of Gaseous Ammonia over Fluorinated TiO_2 with Exposed (001) Facets. *Appl. Catal., B* **2014**, *152-153*, 82−87.

(15) Ong, W.; Tan, L.; Chai, S.; Yong, S.; Mohamed, A. R. Facet-Dependent Photocatalytic Properties of TiO_2-Based Composites for Energy Conversion and Environmental Remediation. *ChemSusChem* **2014**, *7*, 690–719.

(16) Wang, J.; Zhang, P.; Li, X.; Zhu, J.; Li, H. Synchronical Pollutant Degradation and H_2 Production on a Ti^{3+}-doped TiO_2 Visible Photocatalyst with Dominant (001) Facets. *Appl. Catal., B* **2013**, *134-135*, 198−204.

(17) Gordon, T. R.; Cargnello, M.; Paik, T.; Mangolini, F.; Weber, R. T.; Fornasiero, P.; Murray, C. B. Nonaqueous Synthesis of TiO_2 Nanocrystals Using TiF_4 to Engineer Morphology, Oxygen Vacancy Concentration, and Photocatalytic Activity. *J. Am. Chem. Soc.* **2012**, *134*, 6751−6761.

(18) Pan, J.; Liu, G.; Lu, G.; Qing M.; Cheng, H. On the True Photoreactivity Order of {001}, {010}, and {101} Facets of Anatase TiO_2 Crystals. *Angew. Chem. Int. Ed.* **2011**, *50*, 2133–2137.

(19) Roy, N.; Sohn, Y.; Pradhan, D. Synergy of Low-Energy {101} and High-Energy {001} TiO_2 Crystal Facets for Enhanced Photocatalysis. *ACS Nano*, **2013**, *7*, 2532–2540.

(20) Menzel, R.; Duerrbeck, A.; Liberti, E.; Yau, H. C.; McComb, D.; Shaffer, M. S. P. Determining the Morphology and Photocatalytic Activity of Two-Dimensional Anatase Nanoplatelets Using Reagent Stoichiometry. *Chem. Mater.* **2013**, *25*, 2137–2145.

(21) Wang, Z.; Lv, K.; Wang, G.; Deng, K.; Tang, D. Study on the Shape Control and Photocatalytic Activity of High-Energy Anatase Titania. *Appl. Catal., B* **2010**, *100*, 378–385.

(22) Liu, L.; Gu, X.; Ji, Z.; Zou, W.; Tang, C.; Gao, F.; Dong, L. Anion-Assisted Synthesis of TiO_2 Nanocrystals with Tunable Crystal Forms and Crystal Facets and Their Photocatalytic Redox Activities in Organic Reactions. *J. Phys. Chem. C* **2013**, *117*, 18578−18587.

(23) Cargnello, M.; Gordon, T. R.; Murray, C. B. Solution-Phase Synthesis of Titanium Dioxide Nanoparticles and Nanocrystals. *Chem. Rev.* **2014**, *114*, 9319−9345.

(24) Zheng, Y.; Lv, K.; Wang, Z.; Deng, K.; Li, M. Microwave-Assisted Rapid Synthesis of Anatase TiO_2 Nanocrystals with Exposed {001} Facets. *J. Mol. Catal. A: Chem.* **2012**, *356*, 137–143.

(25) Han, X.; Kuang, Q.; Jin, M.; Xie, Z.; Zheng, L. Synthesis of Titania Nanosheets with a High Percentage of Exposed (001) Facets and Related Photocatalytic Properties. *J. Am. Chem. Soc.* **2009**, *131*, 3152–3153.

(26) Yu, J.; Low, J.; Xiao, W.; Zhou, P.; Jaroniec, M. Enhanced Photocatalytic CO_2-Reduction Activity of Anatase TiO_2 by Coexposed {001} and {101} Facets. *J. Am. Chem. Soc*. **2014**, *136*, 8839−8842.

(27) Xiang, Q.; Yu, J.; Jaroniec, M. Tunable Photocatalytic Selectivity of TiO_2 Films Consisted of Flower-like Microspheres with Exposed {001} Facets. *Chem. Commun.* **2011**, *47*, 4532–4534.

(28) Liu, M.; Li, H.; Zeng, Y.; Huang, T. Anatase TiO_2 Single Crystals with Dominant {001} Facets: Facile Fabrication from Ti Powders and Enhanced Photocatalytical Activity. *Appl. Surf. Sci.* **2013**, *274*, 117−123.

(29) Yuan, X.; Gao, B.; Shi, J.; Chen, Y.; Lin, B.; Gu, Z. Morphologically-Tunable Anatase TiO_2 with Exposed (001) Facet and Related Photocatalytic Performance. *Mater. Lett.* **2014**, *128*, 167−169.

(30) Yu, X.; Jeon, B.; Kim, Y. K. Dominant Influence of the Surface on the Photoactivity of Shape-Controlled Anatase TiO_2 Nanocrystals. *ACS Catal.* **2015**, *5*, 3316−3322.

(31) Dozzi, M. V.; Saccomanni, A.; Altomare, M.; Selli, E. Photocatalytic Activity of NH_4F-Doped TiO_2 Modified by Noble Metal Nanoparticle Deposition. *Photochem. Photobiol. Sci.*, **2013**, *12*, 595–601.

(32) Mrowetz, M.; Selli, E. H_2O_2 Evolution during the Photocatalytic Degradation of Organic Molecules on Fluorinated TiO_2. *New J. Chem.* **2006**, *30*, 108–114.

(33) Dozzi, M. V.; Livraghi, S.; Giamello, E.; Selli, E. Photocatalytic Activity of S- and F-Doped TiO_2 in Formic Acid Mineralization. *Photochem. Photobiol. Sci.*, **2011**, *10*, 343–349.

(34) Yang, H. G.; Liu, G.; Qiao, S. Z.; Sun, C. H.; Jin, Y. G.; Campbell Smith, S.; Zou, J.; Cheng, H. M.; Lu, G. Q. Solvothermal Synthesis and Photoreactivity of Anatase TiO_2 Nanosheets with Dominant {001} Facets. *J. Am. Chem. Soc.* **2009**, *131*, 4078−83.

(35) Ye, L.; Liu, J.; Tian, L.; Peng, T.; Zan, L. The Replacement of {101} by {010} Facets Inhibits the Photocatalytic Activity of Anatase TiO_2. *Appl. Catal., B* **2013**, *134−135*, 60−65.

(36) Zhao, X.; Jin, W.; Cai, J.; Ye, J.; Li, Z.; Ma, Y.; Xie, J.; Qi, L. Shape- and Size-Controlled Synthesis of Uniform Anatase TiO_2 Nanocuboids Enclosed by Active {100} and {001} Facets. *Adv. Funct. Mater.* **2011**, *21*, 3554–3563.

(37) Chen, J. S.; Lou, X. W. Anatase TiO_2 nanosheet: An Ideal Host Structure for Fast and Efficient Lithium Insertion/Extraction. *Electrochem. Commun.* **2009**, *11*, 2332–2335.

(38) Wu, X.; Lu, G.; Wang, L. Effect of Sodium on Photovoltaic Properties of Dye-Sensitized Solar Cells Assembled with Anatase TiO_2 Nanosheets with Exposed {001} Facets. *J. Colloid Interface Sci.*, **2013**, *391*, 70–73.

(39) Wu, Q.; Liu, M.; Wu, Z.; Li, Y.; Piao, L. Is Photooxidation Activity of {001} Facets Truly Lower Than That of {101} Facets for Anatase TiO_2 Crystals? *J. Phys. Chem. C*, **2012**, *116*, 26800-26804.

(40) Larson, A. C.; Von Dreele, R. B. General Structure Analysis System (GSAS). Los Alamos National Laboratory Report LAUR 86-748; Los Alamos National Laboratory: Los Alamos, NM, **2004**.

(41) Thompson, P.; Cox, D. E.; Hastings, J. B. Rietveld Refinement of Debye-Scherrer Synchrotron X-ray Data from Al_2O_3. *J. Appl. Crystallogr.* **1987**, *20*, 79−83.

(42) Murakami, N.; Kurihara, Y.; Tsubota, T.; Ohno, T. Shape-Controlled Anatase Titanium(IV) Oxide Particles Prepared by Hydrothermal Treatment of Peroxo Titanic Acid in the Presence of Polyvinyl Alcohol. *J. Phys. Chem. C*, **2009**, *113*, 3062−3069.

(43) Gu, L.; Wang, J.; Cheng, H.; Du, Y.; Han, X. Synthesis of Nano-Sized Anatase TiO_2 with Reactive {001} Facets Using Lamellar Protonated Titanate as Precursor. *Chem. Commun.* **2012**, *48*, 6978–6980.

(44) Coduri, M.; Maisano, M.; Dozzi, M. V.; Selli, E. Morphological Characterization of Shape-Controlled TiO_2 Anatase through XRPD Analysis. *Z. Phys. Chem.* **2016**, doi:10.1515/zpch-2015-0715.

(45) Larson, A.C.; Von Dreele, R.B. GSAS Technical Manual, p 164.

(46) Dozzi, M. V.; Prati, L.; Canton, P.; Selli, E. Effects of Gold Nanoparticles Deposition on the Photocatalytic Activity of Titanium Dioxide under Visible Light. *Phys. Chem. Chem. Phys.* **2009**, *11*, 7171–7180.

(47) Ye, L.; Mao, J.; Liu, J.; Jiang, Z.; Peng, T.; Zan, L. Synthesis of Anatase TiO_2 Nanocrystals with {101}, {001} or {010} Single Facets of 90% Level Exposure and Liquid-Phase Photocatalytic Reduction and Oxidation Activity Orders. *J. Mater. Chem. A* **2013**, *1*, 10532–10537.

(48) Li, G.; Li, L.; Boerio-Goates, J.; Woodfield, B. F. High Purity Anatase TiO_2 Nanocrystals: Near Room-Temperature Synthesis, Grain Growth Kinetics, and Surface Hydration Chemistry. *J. Am. Chem. Soc.* **2005**, *127*, 8659−8666.

(49) Swamy, V.; Menzies, D.; Muddle, B. C.; Kuznetsov, A.; Dubrovinsky, L. S.; Dai, Q.; Dmitriev, V. Nonlinear Size Dependence of Anatase TiO_2 Lattice Parameters. *Appl. Phys. Lett.* **2006**, *88*, 243103

(50) Tian, F.; Zhang, Y.; Zhang, J.; Pan, C. Raman Spectroscopy: A New Approach to Measure the Percentage of Anatase TiO_2 Exposed (001) Facets. *J. Phys. Chem. C* **2012**, *116*, 7515−7519.

(51) Barnard, A. S.; Curtiss, L. A. Prediction of TiO_2 Nanoparticle Phase and Shape Transitions Controlled by Surface Chemistry. *Nano Lett.* **2005**, *5*, 1261−1266.

(52) Lv, K.; Xiang, Q.; Yu, J. Effect of Calcination Temperature on Morphology and Photocatalytic Activity of Anatase TiO_2 Nanosheets with Exposed {001} Facets. *Appl. Catal., B* **2011**, *104*, 275–281.

(53) Sing, K. S. W.; Everett, D. H.; Haul, R. A. W.; Moscou, L.; Pierotti, R. A.; Rouquérol, J.; Siemieniewska, T. Reporting Physisorption Data For Gas/Solid Systems with Special Reference to the Determination of Surface Area and Porosity. *Pure & Appl. Chem.* **1985**, *4*, 603−619.

(54) Yu, J.; Qi, L.; Jaroniec, M. Hydrogen Production by Photocatalytic Water Splitting over Pt/TiO_2 Nanosheets with Exposed (001) Facets. *J. Phys. Chem. C* **2010**, *114*, 13118−13125.

(55) Artiglia, L.; Zana, A.; Rizzi, G. A.; Agnoli, S.; Bondino, F.; Magnano, E.; Cavaliere, E.; Gavioli, L.; Granozzi, G. Water Adsorption on Different TiO_2 Polymorphs Grown as Ultrathin Films on Pt(111). *J. Phys. Chem. C* **2012**, *116*, 12532−12540.

(56) Yu, J. C.; Yu, J.; Ho, W.; Jiang, Z.; Zhang, L. Effects of F^- Doping on the Photocatalytic Activity and Microstructures of Nanocrystalline TiO_2 Powders. *Chem. Mater.* **2002**, *14*, 3808−3816.

(57) Czoska, A. M.; Livraghi, S.; Chiesa, M.; Giamello, E.; Agnoli, S.; Granozzi, G.; Finazzi, E.; Di Valentin, C.; Pacchioni, G. The Nature of Defects in Fluorine-Doped TiO_2. *J. Phys. Chem. C* **2008**, *112*, 8951−8956.

(58) Li, D.; Haneda, H.; Hishita, S.; Ohashi, N.; Labhsetwar, N. K. Fluorine-Doped TiO_2 Powders Prepared by Spray Pyrolysis and their Improved Photocatalytic Activity for Decomposition of Gas-Phase Acetaldehyde. *J. Fluorine Chem.* **2005**, *126*, 69−77.

(59) Li, D.; Ohashi, N.; Hishita, S.; Kolodiazhnyi, T.; Haneda, H. Origin of Visible-Light-Driven Photocatalysis: A Comparative Study on N/F-Doped and N−F-Codoped TiO_2 Powders by Means of Experimental Characterizations and Theoretical Calculations. *J. Solid State Chem.* **2005**, *178*, 3293–3302.

(60) Dozzi, M. V.; Artiglia, L.; Granozzi, G.; Ohtani, B.; Selli, E. Photocatalytic Activity vs Structural Features of Titanium Dioxide Materials Singly Doped or Codoped with Fluorine and Boron. *J. Phys. Chem. C* **2014**, *118*, 25579−25589.

(61) Luan, Y.; Jing, L.; Xie, Y.; Sun, X.; Feng, Y.; Fu, H. Exceptional Photocatalytic Activity of 001-Facet-Exposed TiO_2 Mainly Depending on Enhanced Adsorbed Oxygen by Residual Hydrogen Fluoride. *ACS Catal.* **2013**, *3*, 1378−1385.

(62) Li, C.; Koenigsmann, C.; Ding, W.; Rudshteyn, B.; Yang, K. R.; Regan, K. P.; Konezny, S. J.; Batista, V. S.; Brudvig, G. W.; Schmuttenmaer, C. A.; Kim, J. Facet-Dependent Photoelectrochemical Performance of TiO_2 Nanostructures: An Experimental and Computational Study. *J. Am. Chem. Soc.* **2015**, *137*, 1520−1529.

(63) Bettini, L. G.; Dozzi, M. V.; Della Foglia, F.; Chiarello, G. L.; Selli, E.; Lenardi, C.; Piseri, P.; Milani, P. Mixed-Phase Nanocrystalline TiO_2 Photocatalysts Produced by Flame Spray Pyrolysis. *Appl. Catal., B* **2015**, *178*, 226−232.

(64) Dozzi, M. V.; Chiarello, G. L.; Selli, E. Effects of Surface Modification on the Photocatalytic Activity of TiO_2. *J. Adv. Oxid. Technol.* **2010**, *13*, 305−312.

(65) Mrowetz, M.; Selli, E. Enhanced Photocatalytic Formation of Hydroxyl Radicals on Fluorinated TiO_2. *Phys. Chem. Chem. Phys.* **2005**, *7*, 1100–1102.

(66) Dozzi, M. V.; D'Andrea, C.; Ohtani, B.; Valentini, G.; Selli, E. Fluorine-Doped TiO_2 Materials: Photocatalytic Activity vs Time-Resolved Photoluminescence. *J. Phys. Chem. C* **2013**, *117*, 25586−25595.

(67) Wang, Q.; Chen, C.; Zhao, D.; Wanhong, M.; Zhao, J. Change of Adsorption Modes of Dyes on Fluorinated TiO_2 and Its Effect on Photocatalytic Degradation of Dyes under Visible Irradiation. *Langmuir* **2008**, *24*, 7338−7345.

(68) Dozzi, M. V.; Zuliani, A.; Grigioni, I.; Chiarello, G. L.; Meda, L.; Selli, E. Photocatalytic Activity of one Step Flame-Made Fluorine Doped TiO_2. *Appl. Catal., A* **2015**, doi:10.1016/j.apcata.2015.10.048

ABSTRACT GRAPHIC